Energy-Resolved Ultrashort Delays of Photoelectron Emission Clocked by Orthogonal Two-Color Laser Fields

Xiaochun Gong,[1] Cheng Lin,[2] Feng He,[3] Qiying Song,[1] Kang Lin,[1] Qinying Ji,[1] Wenbin Zhang,[1] Junyang Ma,[1] Peifen Lu,[1] Yunquan Liu,[4] Heping Zeng,[1] Weifeng Yang,[2,*] and Jian Wu[1,5,†]

[1]*State Key Laboratory of Precision Spectroscopy, East China Normal University, Shanghai 200062, China*
[2]*Department of Physics, College of Science, Shantou University, Shantou, Guangdong 515063, China*
[3]*Key Laboratory of Laser Plasmas (Ministry of Education) and Department of Physics and Astronomy, Collaborative Innovation Center for IFSA (CICIFSA), Shanghai Jiao Tong University, Shanghai 200240, China*
[4]*Department of Physics and State Key Laboratory for Mesoscopic Physics, Peking University, Beijing 100871, China*
[5]*Collaborative Innovation Center of Extreme Optics, Shanxi University, Taiyuan, Shanxi 030006, China*

(Received 16 November 2016; revised manuscript received 6 February 2017; published 7 April 2017)

A phase-controlled orthogonal two-color (OTC) femtosecond laser pulse is employed to probe the time delay of photoelectron emission in the strong-field ionization of atoms. The OTC field spatiotemporally steers the emission dynamics of the photoelectrons and meanwhile allows us to unambiguously distinguish the main and sideband peaks of the above-threshold ionization spectrum. The relative phase shift between the main and sideband peaks, retrieved from the phase-of-phase of the photoelectron spectrum as a function of the laser phase, gradually decreases with increasing electron energy, and becomes zero for the fast electron which is mainly produced by the rescattering process. Furthermore, a Freeman resonance delay of 140 ± 40 attoseconds between photoelectrons emitted via the $4f$ and $5p$ Rydberg states of argon is observed.

DOI: 10.1103/PhysRevLett.118.143203

The ultrafast electron dynamics in photoionization is one of the most fundamental processes of light-matter interaction. Attosecond time delays in the photoionization and electron emission from atoms [1,2], molecules [3], and solids [4–6] have been observed. The relative phase shift or the corresponding attosecond time delay of the photoelectron emission [7,8] can be revealed by using the techniques of reconstruction of attosecond beating by interference of two-photon transition [9,10] or the attosecond streak camera [11–15]. The two-photon transition picture in producing the sidebands from the adjacent main peaks [9,10] has been employed to understand the multiphoton ionization process driven by a two-color strong laser field [16]. The ionization potential and thus the photoelectron energies of the above-threshold ionization (ATI) spectrum are ac-Stark shifted [17] by the superposed two-color field, which may lead to an altered energy spectrum as compared to those produced by a single laser field when the fundamental field (FW) and its second harmonic (SH) have comparable intensities. It is hence hard to unambiguously distinguish the photoelectrons of the main and sideband peaks whose relative phase is the key to understanding the electron emission dynamics.

As compared to the photoelectron released directly into the continuum, a remarkable emission delay was recently predicted for the two-photon ionization of Helium when a resonant intermediate state is involved [18]. It is understood as a time delay acquired during the transition via the resonant intermediate state to the continuum, which is denoted as the absorption time delay and related to the energy derivative of the phase that the electron acquired during the transition. As compared to the tunneling time delay [13] or the relative time delay between the photoelectrons emitted from different initial states [1–6], this absorption time delay on the resonant intermediate state is yet experimentally unobserved. Interestingly, in strong-field multiphoton ionization of atoms, the laser field may lift the potential energy of the excited Rydberg state to match the energy of multiple photons of the driving field, i.e., Freeman resonance [19], which provides a ground to experimentally explore the absorption time delay using strong laser fields.

In this Letter, by employing a phase-controlled orthogonal two-color (OTC) femtosecond laser pulse with comparable FW and SH field intensities, spatial- and energy-resolved photoelectron angular distributions (PADs) are measured as a function of the relative phase of the OTC field, allowing us to look into the fine structures and emission dynamics. The phase-of-phase (PP) ϕ_{PP} retrieved from laser phase dependent PADs reveals ultrashort time delays in photoelectron emissions. We observe a Freeman resonance delay of 140 ± 40 attoseconds between the photoelectrons emitted via the $4f$ and $5p$ Rydberg states [schematically illustrated in Fig. 1(a)] of argon (Ar) when they are ac-Stark shifted to be resonant with the energy of multiple photons of the driving fields.

As compared to the parallel polarized two-color laser field, the OTC field steers the photoelectron in both time and space [20–22], which has been extensively used to probe and control many fascinating phenomena. For instance, by adding a weak SH field orthogonally polarized

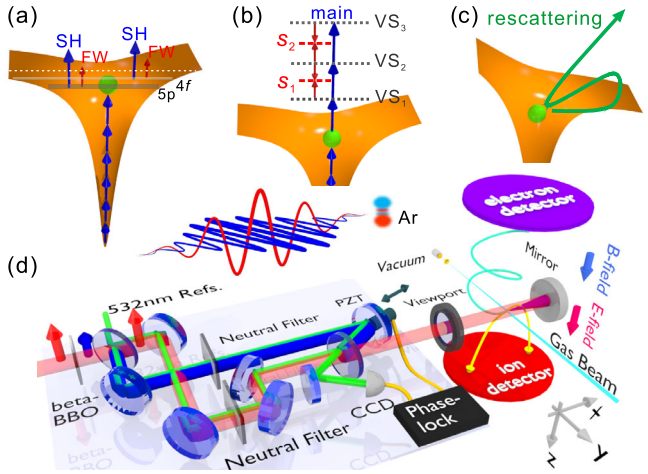

FIG. 1. Schematic illustrations of photoemission dynamics of (a) the Freeman resonance via the field-dressed $5p$ or $4f$ Rydberg states of Ar, (b) the sideband generation from the adjacent main peaks by absorbing or emitting an additional photon via the virtual states (VS) in the continuum, and (c) the field-driving rescattering process. The green bubble and yellow surface stand for the electron and nuclear potential, respectively. (d) Schematic view of experimental setup.

to an intense FW, attosecond recombination timing [23], angstrom length scale atomic orbital [24], and multielectron ionization dynamics [25,26] were probed assisted by high-harmonic spectroscopy [7]. The inter- and intracycle interferences of electrons liberated within one laser cycle or adjacent cycles [27–32] give rise to PADs of rich structures, which could be controlled by adjusting the phase of an OTC field [33,34]. Distinct laser-phase dependences between the emitted slow and fast electrons were anticipated for atoms exposed to an OTC field [35]. Here, we use the phase-controlled OTC field to probe the relative time delay in the photoelectron emissions.

Experimentally, as illustrated in Fig. 1(d), the phase-controlled OTC field was generated using a phase-locked Mach-Zehnder interferometer scheme. An ultraviolet SH pulse was produced by frequency doubling a near-infrared femtosecond laser pulse from a Ti:sapphire multipass amplifier (790 nm, 25 fs, 10 kHz) using a 150-μm-thick β-barium borate (β-BBO) crystal. A phase-locking system [36,37] is employed to finely tune the relative phase (denoted as ϕ_L) between the peaks of the electric fields of the FW and SH of the OTC pulse. The OTC field was tightly focused onto a supersonic gas jet of Ar by a concave silver mirror ($f = 7.5$ cm) in an ultrahigh vacuum chamber of a cold-target recoil-ion momentum spectroscopy setup [38], where the photoionization created ions and electrons were detected in coincidence [39]. The peak intensities of z-polarized FW and y-polarized SH fields in the interaction region were estimated to be $I_{FW} \sim I_{SH} \sim 8.5 \times 10^{13}$ W/cm^2.

Figure 2(a) shows the experimentally measured ϕ_L-integrated PADs correlated to Ar^+ in the y-z plane. Along the y axis ($\phi_e = 0°$ or $\pm 180°$) only main peaks (labeled by white dots) spaced by a SH photon energy are observed, where ϕ_e is the emission angle of the electron in the y-z plane. Additional sidebands differed by the FW photon energy between two adjacent main peaks appear for electrons emitting away from the y axis, e.g., $\phi_e = 30°$ (labeled by black dots). As compared to the ATI spectrum produced by the parallel polarized two-color field where the main peaks and sidebands are both confined along the polarization axis, the OTC field allows us to explicitly identify the sidebands from the main peaks in spite of the ac-Stark shift of the energies of the photoelectrons. The main features of the experimental observations are well reproduced by our three-dimensional generalized quantum trajectory Monte Carlo (GQTMC) simulations [40] as shown in Fig. 2(b). As compared to the quasistatic picture of QTMC simulations [41], the ionization rate and initial exit coordinate of the photoelectron in our GQTMC simulation are optimized by using a nonadiabatic improved Yudin and Ivanov model [42–44] which works well in both tunneling and multiphoton ionization regimes.

Figures 3(a) and 3(e) show the ϕ_L-dependent E_e spectra of electrons emitting to $|\phi_e| < 3°$ and $20° < \phi_e < 40°$, which periodically oscillate versus the laser phase. To increase the visibility of the ϕ_L dependence, we normalized the spectrum of E_e versus ϕ_L as $YN(E_e, \phi_L^i) = Y(E_e, \phi_L^i)/[(1/N)\sum_{\phi_L^1=0}^{\phi_L^N=2\pi} Y(E_e, \phi_L^i)]$, where $Y(E_e, \phi_L^i)$ is the measured electron yield at energy E_e and laser phase ϕ_L, and N is the total number of the scanning step of the laser phase over 2π. The normalized spectra are correspondingly shown in Figs. 3(b) and 3(f), where the ϕ_L-independent background due to the ionization solely by the

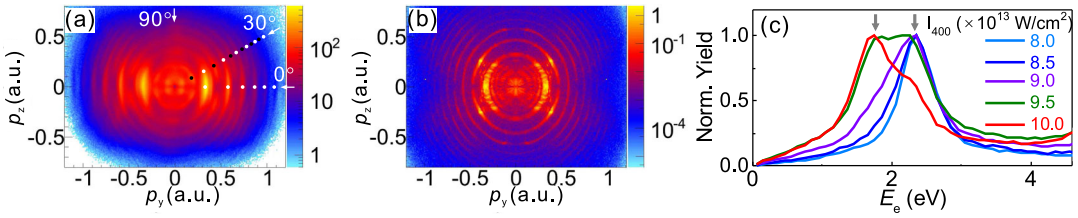

FIG. 2. (a) Measured PADs in y-z plane $|\theta_x - 90°| < 20°$ and (b) simulated PADs integrated over ϕ_L, where θ_x is the azimuth angle with respect to x axis. The white and black dots in (a) denote the main and sideband peaks, respectively. (c) Measured photoelectron spectra at various intensities of the SH field, where E_e is the kinetic energy release of the emitted electron.

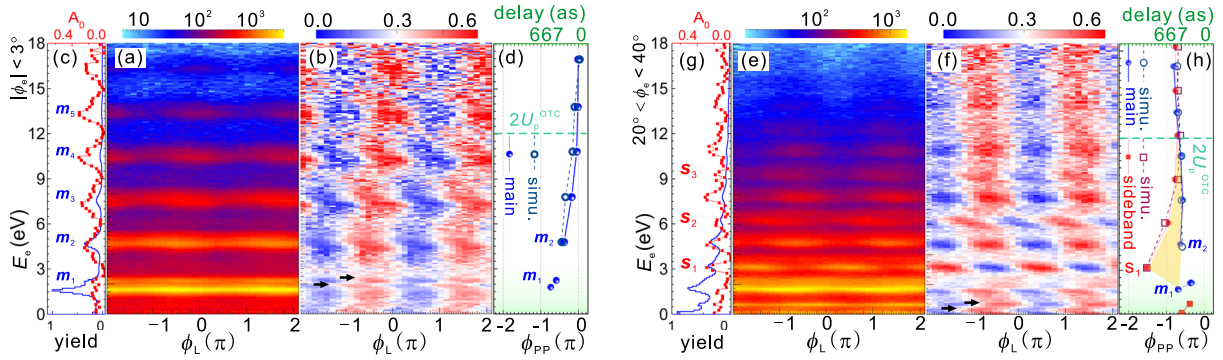

FIG. 3. (a),(e) Measured and (b),(f) normalized 2D spectra of E_e vs ϕ_L. (c),(g) Measured ϕ_L-integrated E_e distribution (blue solid curves) and retrieved contrast amplitude A_0 (red dashed curves). (d),(h) Retrieved phase-of-phase ϕ_{PP} of main (blue solid circles) and sideband peaks (red solid squares). The numerically simulated ϕ_{PP} are correspondingly shown as the blue open circles and red open squares. The left and right panels are for electrons emitting to (a)–(d) $|\phi_e| < 3°$ and (e)–(h) $20° < \phi_e < 40°$, respectively. The horizontal green lines in (d),(h) indicate the energy position of $2U_p^{OTC}$.

FW or SH field is suppressed. The photoelectrons around $\phi_e = 0°$ show similar ϕ_L dependence over all electron energy [Fig. 3(b)], while the ϕ_{PP} of the sidebands clearly differ from the adjacent main peaks as a function of the electron energy along $\phi_e = 30°$ [Fig. 3(f)].

By fitting the normalized spectrum with the formula $YN(\phi_L) = Y_0 + A_0 \cos(\phi_L + \phi_{PP})$ for each ATI peak, we retrieved the contrast amplitude A_0 [red dashed curves in Figs. 3(c) and 3(g)] and PP ϕ_{PP} [Figs. 3(d) and 3(h)] of the photoelectron energy spectra [45,46]. As shown in Figs. 3(c) and 3(g), the contrast amplitude A_0, corresponding to the modulation depth of the ϕ_L dependence of the photoelectron emission, is almost the same for different ATI peaks although the measured yield decreases rapidly with the increase of electron energy. The slight bend of ϕ_{PP} over the electron energy of the main peaks shown in Fig. 3(d) indicates the Coulomb correction of the parent ion to the phases of the interfering electron trajectories [16] which becomes insignificant for the fast electron departing rapidly from the nucleus. It is very well reproduced by our GQTMC simulations (open blue circles) as shown in Fig. 3(d).

According to the intuitive interference picture as schematically illustrated in Fig. 1(b), the sidebands are produced by absorbing or emitting an additional photon from the adjacent main peaks via the virtual states, where a direct beating would induce a π-phase shift in the sidebands as compared to the main peaks [2–5]. As shown in Fig. 3(h), the ϕ_{PP} of the sideband s_1 is -1.53π and its adjacent main peaks m_1 and m_2 are -0.69π and -0.63π, respectively. The averaged PP difference $\delta\phi_{PP}$ between s_1 and m_1 (m_2), $\phi_{PP}^{s_1} - (\phi_{PP}^{m_1} + \phi_{PP}^{m_2})/2$, is about 0.87π, as expected, which is well in agreement with our GQTMC simulations [open blue circles and red squares in Fig. 3(h)]. As shown in Fig. 4(a) for $\phi_L = -1.5\pi$, the photoelectron of the main peak around 4.5 eV emitting to $\phi_e \sim 30°$ mostly (75% of the total emission probability) births nearby the maximum of the FW field and node of the SH field with a nonzero initial kinetic energy. On the other hand, as shown in Fig. 4(b), the photoelectron of the adjacent sideband around 3.0 eV emitting in the same direction is mostly liberated nearby the nodes of both the FW and SH fields with a near zero initial kinetic energy at $t_i = 6.5\ T_{SH}$ for our OTC pulse with $\phi_L = -0.5\pi$. Emissions of electrons at different instants within the phase-controlled OTC pulse give rise to the observed phase shift between the sideband and main peaks of the ATI spectrum. The emission of the sideband peak around the nodes of the FW and SH fields in Fig. 4(b) [40,42,47] can be alternatively ascribed to the absorption or emission of an additional photon from the adjacent virtual states in the continuum as illustrated in Fig. 1(b), which does not require a significant field strength as compared to the liberation of a tightly bound electron in multiphoton ionization. Interestingly, the $\delta\phi_{PP}$ between the main peaks

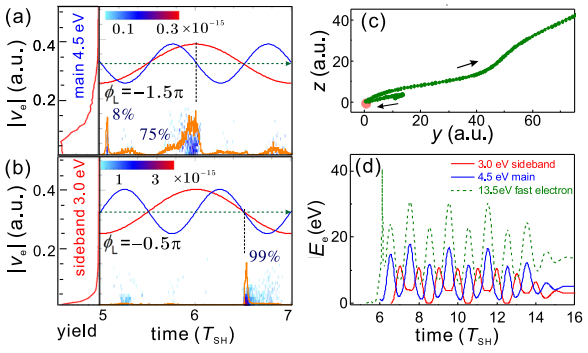

FIG. 4. Simulated birth time tagged ionization rate and initial velocity of (a) main peak at 4.5 eV, (b) sideband peak at 3.0 eV of the photoelectron emitting to $\phi_e \sim 30°$. The red and blue curves denote the electric fields of the FW and SH components of the OTC field. The orange curve is the ionization rate integrated over the initial velocity of the photoelectron, and the distribution of the initial velocity integrated over the emission time is shown in the left panel. (c) The typical trajectory of the fast electron produced via the rescattering process, where the red dot denotes the parent ion at origin. (d) The temporal evolution of the kinetic energy of the liberated photoelectron.

and adjacent sidebands gradually decrease as the electron energy increases along $\phi_e \sim 30°$, and ends up at zero for fast electrons with energy larger than $2U_p^{\mathrm{OTC}} = 2(U_p^{\mathrm{FW}} + U_p^{\mathrm{SH}}) \sim 12$ eV, where $U_p^{\mathrm{FW(SH)}}$ is the ponderomotive energy of a free electron in the FW (SH) laser field.

As compared to the slow electrons, the fast electrons are mostly produced via the rescattering process driven by the laser field as schematically illustrated in Fig. 1(c). Above $2U_p^{\mathrm{OTC}}$ the main and sideband peaks show the same ϕ_{PP} over a wide range of energy as shown in Fig. 3(h). Our GQTMC simulations show that the fast electrons, for instance, around 13.5 and 15.0 eV emitting to the same direction are born within the same tiny time window with a typical rescattering trajectory as shown in Fig. 4(c). It relates to the critical requirement on the initial exit and velocity, ionization time, and recollision angle of the rescattering process for the generation of a fast electron driven by the spatiotemporally shaped OTC pulse. As displayed in Fig. 4(d), the fast electron acquires the main energy from the rescattering as compared to the slow electrons. The gradually decreased $\delta\phi_{\mathrm{PP}}$ between the sidebands and main peaks implies that the rescattering process is more and more dominant in producing the fast electron.

Interestingly, as marked by the horizontal black arrows in Fig. 3(b), two fine peaks with abrupt shift of ϕ_{PP} are observed in m_1 around 2 eV. It corresponds to the bright signal around $p_y = 0.33$ a.u. in Fig. 2(a) and the sharp peaks at 1.75 and 2.18 eV in Fig. 3(a). These two peaks are the photoelectrons emitted via the Freeman resonance [19] of the field-dressed $5p$ and $4f$ Rydberg states of Ar [48,49] populated by absorbing 6 SH photons. The resonant participation of the $5p$ and $4f$ states are determined by examining the electron dipole transition rules, the matching of the energy of multiple photons with the intermediate states, and the observed energy of the photoelectron. Driven by the strong laser field, the potential energy of the Rydberg states may be lifted to be resonant with the energy of multiple photons, on which the electron is considerably populated and afterward transits into the continuum by absorbing one extra photon. Differing from the regular ATI peaks, the energy of the Freeman resonance peak in the photoelectron spectrum is fixed in spite of the variation of the laser intensity. We confirmed it by measuring the photoelectron spectra at different laser intensities driven by the SH field of different peak intensities as shown in Fig. 2(c), where the vertical gray arrows denote the fixed location of the photoelectron produced via the Freeman resonance in multiphoton ionization of Ar [48,49].

As shown in Figs. 3(d) and 3(h), these two Freeman resonance peaks show PP differences of $\delta\phi_{\mathrm{PP}} = \phi_{\mathrm{PP}}^{4f} - \phi_{\mathrm{PP}}^{5p} \sim 0.24\pi$ and 0.42π for $\phi_e = 0°$ and 30°, respectively. It relates to the time delay between two photoionization pathways, i.e., the photoelectrons emitted via the $5p$ and $4f$ intermediate states. For each pathway, the time delay of the photoionization includes the contributions from the multiphoton transition process, the propagation of the photoelectron in the combined field of the atomic potential and the laser field, and the Freeman resonance delay. Here the experimentally measured time delay between two photoionization pathways reveals the important role of the Freeman resonance, in particular the Freeman resonance delay in strong-field multiphoton ionization processes.

To estimate the Freeman resonance delay, we ran the time-dependent Schrödinger equation (TDSE) simulations in parallel to the GQTMC simulations (for details please see Supplemental Material [50]). In the GQTMC simulation, the Freeman resonance is not able to be included while other processes can be well described. However, both the experimental and TDSE results include the Freeman resonance, as well as other processes already covered by the GQTMC simulation. Thus, one may expect the time delay obtained from the experiment and TDSE results subtracting the time delay obtained from the GQTMC simulation tells us that the time delay comes from the Freeman resonance. For photoelectrons emitting to $\phi_e = 0°$ and $\phi_e = 30°$, the phase differences between the TDSE (experiments) and GQTMC simulations are $\delta\phi_{\mathrm{PP}}^{\mathrm{TDSE}} - \delta\phi_{\mathrm{PP}}^{\mathrm{GQTMC}} = 0.14\pi$ and 0.13π and $\delta\phi_{\mathrm{PP}}^{\mathrm{Exp}} - \delta\phi_{\mathrm{PP}}^{\mathrm{GQTMC}} = 0.19\pi$ and 0.22π, respectively. This averaged phase difference of $0.21\pi \sim (0.19\pi + 0.22\pi)/2$ corresponds to a difference of 140 ± 40 attoseconds of the Freeman resonance delay between the photoelectrons emitted via the $5p$ and $4f$ states in our experiments by comparing them with the GQTMC simulations. The divergence of the TDSE simulation from the experiment might be because that the TDSE simulation we employed is two-dimensional in space without considering intensity averaging in the focusing volume. It is physically reasonable that the Freeman resonance delay between two photoionization pathways should be insensitive to the photoelectron emission direction. On the other hand, the different phase differences $\delta\phi_{\mathrm{PP}}^{\mathrm{GQTMC}} = 0.05\pi$ and 0.2π for photoelectrons emitting to $\phi_e = 0°$ and $\phi_e = 30°$ imply the influence of the Coulomb correction. As indicated in Fig. 3(f) and shown in Fig. 3(h), a similar PP difference is observed in the sideband at 0.14 eV and 0.65 eV as compared to those in m_1 for electrons emitting to $\phi_e \sim 30°$.

In summary, we experimentally observed a 140 ± 40 attoseconds difference of the Freeman resonance delay between the photoelectrons emitted via the field-dressed $4f$ and $5p$ states of Ar atom. The OTC field spatiotemporally steers the photoelectron emission, which meanwhile allows us to unambiguously distinguish the main and sideband peaks of the ATI spectrum. The phase shift between the sideband and main peaks gradually decreases from π to zero with the increasing of the electron energy, which indicates different emission dynamics in different ranges of photoelectron energy spectra. Our findings advance the understanding of subcycle photoelectron emission

dynamics, and shed new light on the accurate control of ultrafast electron dynamics in light-matter interactions.

We thank X. Xie, X. Song, M. Liu, P. He, H. J. Wörner, and C. Nam for the fruitful discussions. This work is supported by National Natural Science Fund (Grants No. 11425416, No. 11374202, No. 11322438, No. 11621404, and No. 61690224), and the 111 project of China (Grant No. B12024).

*wfyang@stu.edu.cn
†jwu@phy.ecnu.edu.cn

[1] M. Schultze *et al.*, Science **328**, 1658 (2010).
[2] K. Klünder *et al.*, Phys. Rev. Lett. **106**, 143002 (2011).
[3] M. Huppert, I. Jordan, D. Baykusheva, A. von Conta, and H. J. Wörner, Phys. Rev. Lett. **117**, 093001 (2016).
[4] R. Locher, L. Castiglioni, M. Lucchini, M. Greif, L. Gallmann, J. Osterwalder, M. Hengsberger, and U. Keller, Optica **2**, 405 (2015).
[5] Z. Tao, C. Chen, T. Szilvási, M. Keller, M. Mavrikakis, H. Kapteyn, and M. Murnane, Science **353**, 62 (2016).
[6] A. L. Cavalieri *et al.*, Nature (London) **449**, 1029 (2007).
[7] F. Krausz and M. Ivanov, Rev. Mod. Phys. **81**, 163 (2009).
[8] R. Pazourek, S. Nagele, and J. Burgdörfer, Rev. Mod. Phys. **87**, 765 (2015).
[9] P. M. Paul, E. S. Toma, P. Breger, G. Mullot, F. Augé, Ph. Balcou, H. G. Mulller, and P. Agostini, Science **292**, 1689 (2001).
[10] H. G. Muller, Appl. Phys. B **74**, S17 (2002).
[11] J. Itatani, F. Quéré, G. L. Yudin, M. Yu. Ivanov, F. Krausz, and P. B. Corkum, Phys. Rev. Lett. **88**, 173903 (2002).
[12] C. M. Maharjan, A. S. Alnaser, X. M. Tong, B. Ulrich, P. Ranitovic, S. Ghimire, Z. Chang, I. V. Litvinyuk, and C. L. Cocke, Phys. Rev. A **72**, 041403(R) (2005).
[13] P. Eckle, A. N. Pfeiffer, C. Cirelli, A. Staudte, R. Dörner, H. G. Muller, M. Büttiker, and U. Keller, Science **322**, 1525 (2008).
[14] X. Wang, J. Tian, and J. H. Eberly, Phys. Rev. Lett. **110**, 243001 (2013).
[15] L. Torlina *et al.*, Nat. Phys. **11**, 503 (2015).
[16] L. J. Zipp, A. Natan, and P. H. Bucksbaum, Optica **1**, 361 (2014).
[17] P. Agostini, P. Breger, A. L'Huillier, H. G. Muller, G. Petite, A. Antonetti, and A. Migus, Phys. Rev. Lett. **63**, 2208 (1989).
[18] J. Su, H. Ni, A. Jaroń-Becker, and A. Becker, Phys. Rev. Lett. **113**, 263002 (2014).
[19] R. R. Freeman, P. H. Bucksbaum, H. Milchberg, S. Darack, D. Schumacher, and M. E. Geusic, Phys. Rev. Lett. **59**, 1092 (1987).
[20] M. Kitzler and M. Lezius, Phys. Rev. Lett. **95**, 253001 (2005).
[21] L. Brugnera, D. J. Hoffmann, T. Siegel, F. Frank, A. Zaïr, J. W. G. Tisch, and J. P. Marangos, Phys. Rev. Lett. **107**, 153902 (2011).
[22] X. Xie, Phys. Rev. Lett. **114**, 173003 (2015).
[23] D. Shafir, H. Soifer, B. D. Bruner, M. Dagan, Y. Mairesse, S. Patchkovskii, M. Yu. Ivanov, O. Smirnova, and N. Dudovich, Nature (London) **485**, 343 (2012).
[24] D. Shafir, Y. Mairesse, D. M. Villeneuve, P. B. Corkum, and N. Dudovich, Nat. Phys. **5**, 412 (2009).
[25] H. Niikura, H. J. Wörner, D. M. Villeneuve, and P. B. Corkum, Phys. Rev. Lett. **107**, 093004 (2011).
[26] H. Yun, K.-M. Lee, J. H. Sung, K. T. Kim, H. T. Kim, and C. H. Nam, Phys. Rev. Lett. **114**, 153901 (2015).
[27] F. Lindner, M. G. Schätzel, H. Walther, A. Baltuška, E. Goulielmakis, F. Krausz, D. B. Milošević, D. Bauer, W. Becker, and G. G. Paulus, Phys. Rev. Lett. **95**, 040401 (2005).
[28] R. Gopal *et al.*, Phys. Rev. Lett. **103**, 053001 (2009).
[29] D. G. Arbó, K. L. Ishikawa, K. Schiessl, E. Persson, and J. Burgdörfer, Phys. Rev. A **81**, 021403(R) (2010).
[30] Y. Huismans *et al.*, Science **331**, 61 (2011).
[31] X.-B. Bian, Y. Huismans, O. Smirnova, K.-J. Yuan, M. J. J. Vrakking, and A. D. Bandrauk, Phys. Rev. A **84**, 043420 (2011).
[32] X. Xie *et al.*, Phys. Rev. Lett. **108**, 193004 (2012).
[33] M. Richter, M. Kunitski, M. Schöffler, T. Jahnke, L. P. H. Schmidt, M. Li, Y. Liu, and R. Dörner, Phys. Rev. Lett. **114**, 143001 (2015).
[34] J. W. Geng, W. H. Xiong, X. R. Xiao, L. Y. Peng, and Q. Gong, Phys. Rev. Lett. **115**, 193001 (2015).
[35] J. Henkel and M. Lein, Phys. Rev. A **92**, 013422 (2015).
[36] M. Chini, H. Mashiko, H. Wang, S. Chen, C. Yun, S. Scott, S. Gilbertson, and Z. Chang, Opt. Express **17**, 21459 (2009).
[37] K. Lin *et al.*, J. Phys. B **49**, 025603 (2016).
[38] J. Ullrich, R. Moshammer, A. Dorn, R. Dörner, L. Ph. H. Schmidt, and H. Schmidt-Böcking, Rep. Prog. Phys. **66**, 1463 (2003).
[39] O. Jagutzki *et al.*, IEEE Trans. Nucl. Sci. **49**, 2477 (2002).
[40] X. Song, C. Lin, Z. Sheng, P. Liu, Z. Chen, W. Yang, S. Hu, C. D. Lin, and J. Chen, Sci. Rep. **6**, 28392 (2016).
[41] M. Li, J. Geng, H. Liu, Y. Deng, C. Wu, L. Y. Peng, Q. Gong, and Y. Liu, Phys. Rev. Lett. **112**, 113002 (2014).
[42] G. L. Yudin and M. Yu. Ivanov, Phys. Rev. A **64**, 013409 (2001).
[43] A. M. Perelomov, V. S. Popov, and M. V. Terent'ev, Sov. Phys. JETP **23**, 924 (1966).
[44] D. I. Bondar, Phys. Rev. A **78**, 015405 (2008).
[45] X. Gong, P. He, Q. Song, Q. Ji, H. Pan, J. Ding, F. He, H. Zeng, and J. Wu, Phys. Rev. Lett. **113**, 203001 (2014).
[46] S. Skruszewicz, J. Tiggesbäumker, K.-H. Meiwes-Broer, M. Arbeiter, Th. Fennel, and D. Bauer, Phys. Rev. Lett. **115**, 043001 (2015).
[47] M. Klaiber and J. S. Briggs, Phys. Rev. A **94**, 053405 (2016).
[48] C. M. Maharjan, A. S. Alnaser, I. Litvinyuk, P. Ranitovic, and C. L. Cocke, J. Phys. B **39**, 1955 (2006).
[49] R. R. Freeman and P. H. Bucksbaum, J. Phys. B **24**, 325 (1991).
[50] See Supplemental Material at http://link.aps.org/supplemental/10.1103/PhysRevLett.118.143203, which includes Refs. [51], for details of the simulation and estimation of the Freeman resonance delay.
[51] W. Yang, H. Zhang, C. Lin, J. Xu, Z. Sheng, X. Song, S. Hu, and J. Chen, Phys. Rev. A **94**, 043419 (2016).